

Chapter 2

Fundamentals and Techniques

2.1 X-Ray Photoelectron Spectroscopy (XPS)

Photoelectron spectroscopy makes use of the photoelectric effect, which was discovered in 1887 by Hertz and explained by Einstein in 1905 [1]. When a material is irradiated with light whose energy $h\nu$ exceeds the material's work function (usually a few electron volts, depending on the sample material), electrons are ejected from the material. The photoelectron leaves the sample with a defined kinetic energy E_{kin} , which can be measured with an energy dispersive electron analyser (e.g., a hemispherical analyser). Through knowledge of E_{kin} of the photoelectron, the binding energy (BE) E_B relative to the vacuum level can be calculated according to the Einstein equation:

$$E_B^V = h\nu - E_{kin} \quad (2.1)$$

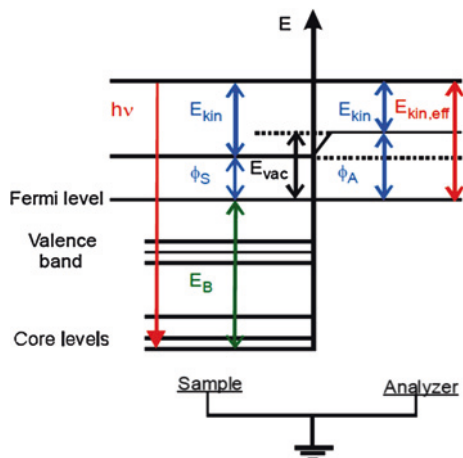
While for gas phase species equation (2.1) is valid, for condensed matter the work functions of both the sample (ϕ_s , variable) and the electron analyser (ϕ_{spec} , constant) have to be considered as they influence E_{kin} , (see Scheme 2.1 for details). This reference problem is usually overcome by calibrating the spectrometer to the Fermi level of the (conducting) sample, which can be achieved by direct measurement of the Fermi level (for example in the case of Ni) or a characteristic signal of high intensity and narrow natural line width (such as the Au 4f_{7/2} level), leading to Eq. (2.2):

$$E_B^V = h\nu - E_{kin} - \phi_{spec} = h\nu - E_{kin}^{eff} \quad (2.2)$$

In the absence of such a defined reference level, other arbitrary internal reference levels can be defined, in most cases leading to less accurate absolute BE positions.

During the photoemission process, interactions of the photoelectrons with the surrounding matter can take place. Typical interactions are inelastic scattering, vibrational or other electronic excitations. A photoelectron may undergo multiple "energy loss events" leading to both lower kinetic energies of the primary electron and also the generation of secondary electrons, resulting in a superimposed

Scheme 2.1 Schematic energy diagram for X-ray photoelectron spectroscopy [2–4]



background signal. The spectral lines observed in a typical XP spectrum, however, are due to the discrete energy values of the core levels of the elements present in the sample, therefore making XPS an element specific technique. Furthermore, each core level has a constant excitation cross section at given $h\nu$, which allows for quantitative analysis, also leading to the expression “electron spectroscopy for chemical analysis” (ESCA). Quantitative analysis is possible when the transmission function of the electron analyser is known, which can be easily calibrated by using ILs such as $[\text{C}_2\text{C}_1\text{Im}][\text{Tf}_2\text{N}]$, due to the presence of a variety of different elements evenly distributed over the whole BE range probed by a standard x-ray gun. As signal and background intensity are dependent of a variety of parameters such as sample position (with respect to both x-ray gun and analyser), photon flux and detection angle, correction factors can be applied to compensate for intensity variations and therefore allow for quantitative comparison of spectra taken at different detection angles (see below) [5]. A typical XPS survey spectrum of a clean Au(111) single crystal and an ionic liquid, in this case $[\text{C}_8\text{C}_1\text{Im}][\text{Tf}_2\text{N}]$, is shown in Fig. 2.1.

Although the core electrons of an atom are not directly involved in a chemical bond, they are still influenced by the chemical surrounding of the atom. Consequently, the BE depends on the chemical state of a compound, leading to a chemical shift of the core level signal, which can amount to BE shifts of several eV. Typically, this effect can be divided into so-called initial state and final state effects. The terms initial and final state refer to the respective energies in the photoemission process resulting in the measured BE [2]:

$$E_B = E_f^{N-1} - E_i^N \quad (2.3)$$

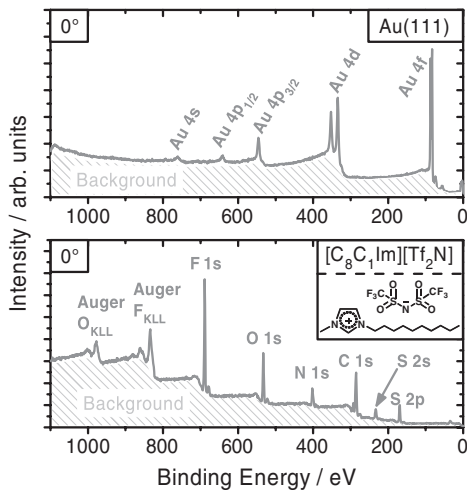
with:

E_i^N Energy of the initial state with N electrons

E_f^{N-1} Energy of the final state with N – 1 electrons.

A typical initial state effect is given by a permanent partial charge at the emitting atom, for example through chemical bonding to another atom. When this atom

Fig. 2.1 XPS survey scans of an Au(111) single crystal and the IL $[\text{C}_8\text{C}_1\text{Im}][\text{Tf}_2\text{N}]$



is probed, the kinetic energy of the emitted photoelectron is higher for a negative and lower for a positive partial charge, due to higher/lower Coulomb interactions. A typical final state effect is a more efficient screening of the core hole or more efficient relaxation by surrounding electrons. Such more effective screening leads to a higher kinetic energy of the photoelectron as the positive core hole is not interacting as strongly with the emitted photoelectron, resulting in a lower BE value. Another feature in XP spectra is the appearance of “shake off” and “shake up” satellites, which can also be assigned to the subgroup of final state effects. A more detailed description of these phenomena can be found in References [2, 3, 6]. Furthermore, an excited core hole created in the photoemission process can undergo an Auger decay resulting in an Auger electron with a characteristic kinetic energy independent of the incident photon energy. Therefore, Auger peaks are a common (but often undesired) feature in an XP spectrum, as can be seen in Fig. 2.1.

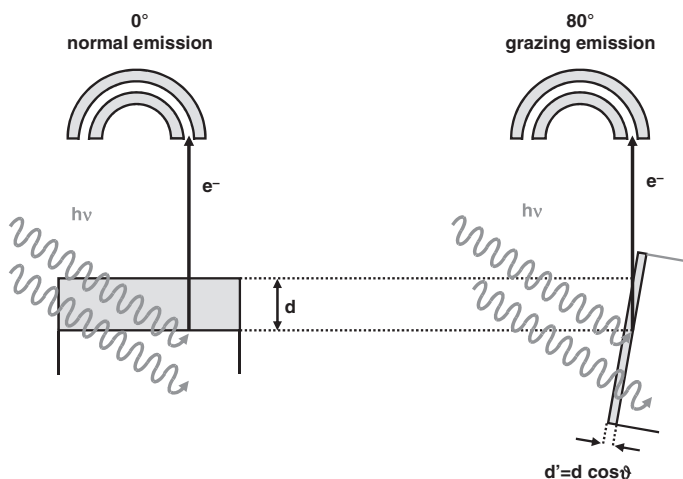
The excited photoelectrons have a very high cross section with condensed matter, which makes XPS an inherently surface sensitive method. Due to inelastic scattering processes described above fewer electrons from deeper layers can leave the sample surface without undergoing some kind of energy loss process. The mean distance an electron can travel without an inelastic scattering event is given by the inelastic mean free path λ , which is a function of the kinetic energy of the respective electron and also depends on the nature (atomic number and density) of the material it passes through. For the organic materials and the kinetic energies used in this study λ is estimated to be 2–3 nm [7, 8]. The maximum information depth of 6–9 nm can be calculated from Eq. (2.4), where the signal intensity I_0 is damped to I_d when covered by an overlayer of a certain thickness d .

$$I_d = I_0 \cdot e^{-d/\lambda} \cdot \cos \vartheta \quad (2.4)$$

with ϑ : electron take-off angle with respect to the surface normal.

Equation (2.4) can also be used to estimate the film thickness and to analyse the growth behaviour of a compound deposited on top of a support material. For strict layer-by-layer growth a polygon-like behaviour along the exponential line should be observed, as until completion of one closed layer (with a defined thickness given by the dimensions of the deposit), a linear decrease should be observed until the next layer starts to grow (see Ref. [9] for details). Further information on the growth behaviour can be extracted when measuring in an angle-resolved XPS (ARXPS) setup. In ARXPS the surface sensitivity can be enhanced by the cosine of the electron take-off angle relative to the surface normal, as depicted in Scheme 2.2. By comparing the signal damping in normal and grazing emission, the growth behaviour can be analysed in such a way, that it is even possible to distinguish between Frank-van-der-Meerve (layer-by-layer growth) and Stranski–Krastanov (2D-wetting layer followed by island growth) growth mechanisms, which will be shown in this thesis (see Chaps. 4 and 5).

However, ARXPS is not only advantageous for the determination of the growth behaviour of deposits. In fact, it is a very powerful tool for the investigation of surface enrichment effects within the top most layers of a compound, which is achieved by comparing the relative normal and grazing emission intensities of the species (i.e., an element or parts of a molecule) present in the topmost layers of the sample. If the grazing emission intensity of a certain species A is increased at the expense of another species B compared to the XPS intensities under normal emission geometry, it can be concluded that A is enriched at the surface. This is elucidated in Fig. 2.2, where the enrichment of the C₁₀ alkyl chain of [C₁₀C₁Im][Tf₂N] is compared to the non-enriched oligo(etherglycol) chains of [Me(EG)₃C₁Im][Tf₂N] [10].



Scheme 2.2 Illustration of the ARXPS setup. The information depth d' results from the cosine of the tilt angle with respect to the surface normal, therefore at 80° the surface sensitivity of XPS can be enhanced by a factor of six

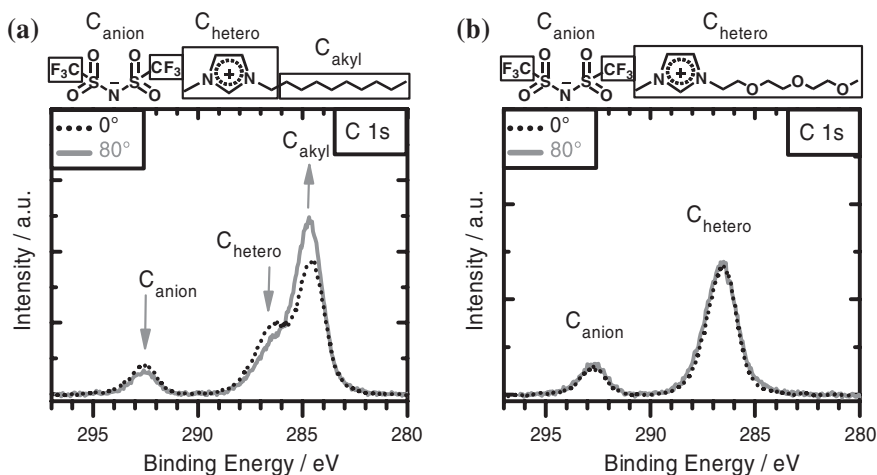


Fig. 2.2 Comparison of ARXP spectra of **a** [C₁₀C₁Im][Tf₂N] and **b** [Me(EG)₃C₁Im][Tf₂N]. In **a** an unambiguous increase of C_{alkyl} and a concomitant decrease of C_{anion} and C_{hetero} is observed in 80° emission. For **b**, however, no relative changes are observed. For a detailed assignment of spectral features in the C 1s region, see Sect. 2.2, for a more detailed discussion of the surface structure of [C_nC₁Im][Tf₂N] ILs, see Ref. [10] and Sect. 3.2. Note, that the 80° emission data have been normalized using a geometry factor to allow for visual comparison, see Ref. [5] for details

2.2 Ionic Liquids

As already mentioned in the Introduction, ILs are a new class of materials with unique physico-chemical properties. The concept of molten salts, however, has been around for a long time and it has been shown that in some well-established industrial processes (vanadia-based catalysts for sulphuric acid production and flue gas cleaning, see Ref. [11] and references therein) the heterogeneous catalyst is in fact a molten salt under reaction conditions. Also, in aluminium smelters, a eutectic mixture of alumina (Al₂O₃) and Kryolithe (Na₃[AlF₆]) is used as the electrolyte from which metallic Al is cathodically deposited. However, examples for the use of molten salts are rare and usually require high energy input (due to the high melting points). In addition, high temperature salt melts are usually strongly corrosive and thus extremely hazardous and difficult to handle. While the first representative of a room temperature IL (RTIL) was synthesized and characterized almost 100 years ago by Paul Walden [12], it was not until the late second half of the twentieth century that the potential of these materials was recognized and the term “Ionic Liquid” was coined. While the early generation of ILs still had numerous disadvantageous properties such as air- and water-sensitivity, research efforts by Wilkes led to the development of easy-to-handle air- and water-stable ILs [13, 14].

After this, as ILs became readily available to a lot of fields, IL research progressed into new realms. Already after a few years a broad range of IL-based

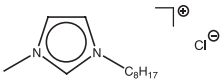
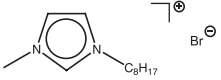
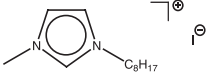
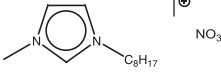
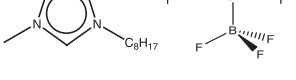
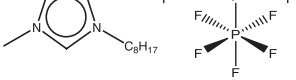
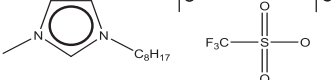
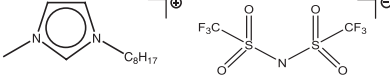
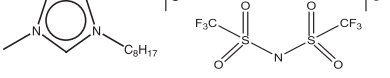
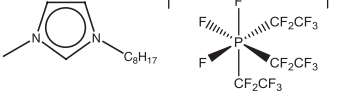
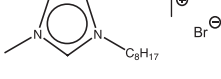
research fields had developed, which is mainly due to the fact that because of the diversity of possible IL structures an almost unlimited number of different ILs can be synthesized [15]. This led to the terms “task-specific” ILs and “designer solvents” and accounts for the fact that by changing the chemical structure of an IL the physico-chemical properties can be adjusted according to the boundary conditions given by the desired application. An overview of a few common cations and anions that ILs can be composed of is shown in Fig. 1.1.

Although the structural diversity has enormous and exciting potential for future applications, it is also disadvantageous from a fundamental point of view. The physico-chemical properties of ILs can be tuned in such a wide range and are therefore so manifold that so far quite often a thorough understanding of the structure-performance relationship is lacking and systematic trends have yet to be developed. However, in the fields of fundamental IL research addressing the physico-chemical properties of ILs there is one IL, namely $[\text{C}_n\text{C}_1\text{Im}][\text{Tf}_2\text{N}]$, which could be considered the “guinea pig” of IL research, being by far the best-investigated IL system. Also in this thesis, mainly imidazolium-based ILs are investigated; in Chap. 3 $[\text{C}_8\text{C}_1\text{Im}]^+$ -based cations are paired with different anions, while $[\text{C}_n\text{C}_1\text{Im}][\text{Tf}_2\text{N}]$ is, apart from one pyrrolidinium IL, exclusively used in Chaps. 4 and 5. An overview of the ILs used in this thesis is given in Table 2.1. As the imidazolium cation and the $[\text{Tf}_2\text{N}]^-$ anion are mainly used, some important fundamental properties of these two ions shall be reviewed followed by a brief description of their “bulk” XP spectra.

Starting with the imidazolium cation, the most striking feature in its chemical structure is the aromatic ring system, where the positive charge is delocalized leading to a relatively low average charge density. This property is of fundamental relevance for forming an IL, as it prevents build-up of a stable crystal lattice by allowing multiple low energy conformations. Delocalized positively charged moieties are found for a variety of other cations. Another structural motif leading to reduced melting points is found in systems, where the positive centre is surrounded by bulky alkyl substituents (i.e. $[\text{NR}_4]^+$) and is thus sterically inaccessible by the anion. For the imidazolium cation, alkyl chains of usually different length (usually one methyl group ($m = 1$) and one alkyl chain with $1 \leq n \leq 10$) are attached to the two nitrogen atoms. The positive charge does not penetrate very far into the alkyl chain, resulting in a rather neutral part of the ion (see also Sect. 3.1 for a detailed discussion). While generally distinct alterations in the physico-chemical properties of an IL can be achieved by changing the ion backbone, i.e., the cationic headgroup/charged moiety of the cation and by changing the anion, fine tuning of the resultant IL is usually achieved by changing the length of the alkyl chains attached to the ionic part of the cation [16]. In a further step, functional groups can be introduced into these side chains leading to even more structural diversity and higher abundance of individually tuneable properties.

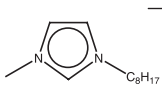
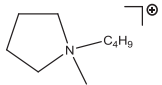
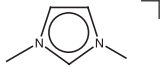
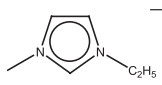
For imidazolium-based ILs, three main intermolecular interaction modes with the counter ion (or other species such as dissolved molecules or surface atoms in contact with the IL) can be identified: Coulombic, dispersive and hydrogen-bonding interactions. Coulombic interactions are long range interactions that fall

Table 2.1 Overview of al ILs investigated in this thesis

Label	Structure	Name	Chapter #
[C ₈ C ₁ Im]Cl		1-methyl-3-octyl-imidazolium chloride	3
[C ₈ C ₁ Im]Br		1-methyl-3-octyl-imidazolium bromide	3
[C ₈ C ₁ Im]I		1-methyl-3-octyl-imidazolium iodide	3
[C ₈ C ₁ Im][NO ₃]		1-methyl-3-octyl-imidazolium nitrate	3
[C ₈ C ₁ Im][BF ₄]		1-methyl-3-octyl-imidazolium tetrafluoroborate	3
[C ₈ C ₁ Im][PF ₆]		1-methyl-3-octyl-imidazolium hexafluorophosphate	3
[C ₈ C ₁ Im][TfO]		1-methyl-3-octyl-imidazolium trifluoromethylsulfonate	3
[C ₈ C ₁ Im][Tf ₂ N]		1-methyl-3-octyl-imidazolium bis[(trifluoromethyl)sulfonyl]imide	3, 4
[C ₈ C ₁ Im][Pf ₂ N]		1-methyl-3-octyl-imidazolium bis[(pentafluoroethyl)sulfonyl]imide	3
[C ₈ C ₁ Im][FAP]		1-methyl-3-octyl-imidazolium tris(pentafluoroethyl)-trifluorophosphate	3
[C ₈ C ₁ C ₁ Im]Br		1,2-methyl-3-octyl-imidazolium bromide	3

(continued)

Table 2.1 (continued)

Label	Structure	Name	Chapter #
[C ₈ C ₁ Im] [Tf ₂ N]		1,2-methyl-3-octylimidazolium bis[(trifluoromethyl)sulfonyl]imide	3
[C ₄ C ₁ Pyrr] [Tf ₂ N]		1-Butyl-1-methylpyrrolidinium bis[(trifluoromethyl)sulfonyl]imide	4
[C ₁ C ₁ Im][Tf ₂ N]		1,3-dimethylimidazolium bis[(trifluoromethyl)sulfonyl]imide	4, 5
[C ₂ C ₁ Im][Tf ₂ N]		1-ethyl-3-methylimidazolium bis[(trifluoromethyl)sulfonyl]imide	5

Displayed are their label used throughout this thesis, their chemical structure, IUPAC name, and the chapter in which the respective IL is investigated

off with $1/r$, leading to some kind of long range order, even in the liquid phase of ILs. Dispersive forces are of much shorter range and taper off with $1/r^6$, yet, theoretical calculations show that dispersive interactions play a crucial role for the liquidity of ILs as they create more shallow energy potential curves compared to solid salts such as NaCl [17]. The dispersive interactions discussed here actually address dispersive forces within the charged regions of the molecules, as they are usually large and have a strongly delocalized excess charge. Contributions through dispersive forces by the alkyl chains—usually referred to as van der Waals interactions—have to be taken into account, too; however, these interactions eventually lead to increased melting points. Therefore, the influence of alkyl chain length on the melting point of the IL has to be subdivided into two parts, namely the symmetry breaking region ranging from C₂–C₈ where decreased melting points are observed, and the hydrophobic region \geq C₁₀, where melting points are drastically increased due to increasing dispersive forces between the alkyl chains [18]. While imidazolium-ILs with short alkyl chains ($n < 4$) have a homogenous structure with alternating ions, it was shown that for longer alkyl chains domains develop where non-polar alkyl chains and charged headgroups segregate and create micro-heterogeneities [19]. This concept holds true for all ILs containing longer aliphatic carbon chains. A similar trend is observed for the IL/vacuum (and the IL/air) interface, where for $n \geq 4$ an alkyl-dominated surface layer develops, as has been shown in a recent XPS study performed by our group [10]. Therein, it could be shown that for [C_nC₁Im][Tf₂N] (with $1 \leq n \leq 16$) stronger surface enrichment of the alkyl chain is found with increasing alkyl chain length (see Fig. 3.14 in Sect. 3.2). Hydrogen bonds have—as the name implies—a localized bond-like structure and have to be considered in imidazolium ILs because the proton in

the C₂ position of the imidazolium ring exhibits a certain acidity ($\text{pK}_a \sim 24$ for $[\text{C}_1\text{C}_1\text{Im}]^+$ [20], compared to ~ 16 for EtOH and >40 for butane). A measure for the hydrogen bond donor ability of the cation is given by the Kamlet-Taft parameter α . Nonetheless, the extent to which hydrogen bonding can take place also depends on the nature of the anion, i.e., its hydrogen bond basicity (Kamlet-Taft parameter β), which is closely related to the availability of localized electron lone pairs and therefore increases with decreasing strength of the conjugate acid of the anion. Further aspects dealing with electrostatic and hydrogen-bonding forces in imidazolium ILs are discussed in more detail in [Chap. 3](#).

The $[\text{Tf}_2\text{N}]^-$ anion with its very bulky yet highly flexible low symmetry structure (apart from one conformer with C₂ symmetry, all other structures have C₁ symmetry) has the negative charge distributed fairly evenly over the whole $[\text{O}_2\text{S}-\text{N}-\text{SO}_2]$ moiety of the molecule, with slightly less charge density at the electron-withdrawing CF₃ groups [21]. Furthermore, access to the $[\text{S}-\text{N}-\text{S}]^-$ centre is hindered due to steric shielding by the surrounding triflate groups [22]. There are a number of low energy conformations leading to a variety of almost energetically degenerate conformations at room temperature, which help to prevent the formation of a stable crystal lattice, eventually leading to reduced melting points. Broadly speaking it can be said that $[\text{Tf}_2\text{N}]^-$ -based ILs are rather hydrophobic, chemically inert and thermally stable, and are therefore most widely used [22]. In XPS, as derived from our own experience, $[\text{Tf}_2\text{N}]^-$ -based ILs exhibit relatively few X-ray radiation-induced decomposition effects compared to other anions such as $[\text{BF}_4]^-$ or $[\text{FAP}]^-$. Also, no water adsorption on the IL surface or in the IL bulk is observed during XPS, which can be the case for strongly hydrophilic ILs such as $[\text{C}_n\text{C}_m\text{Im}]\text{Cl}$. Furthermore, $[\text{Tf}_2\text{N}]^-$ ILs can be evaporated under UHV conditions well below their decomposition temperature and are therefore ideal candidates for the IL-PVD process used in the thin films experiments presented in [Chaps. 4 and 5](#).

At this point, it seems relevant to discuss the spectral features that a prototypical IL used throughout this thesis, namely $[\text{C}_8\text{C}_1\text{Im}][\text{Tf}_2\text{N}]$, gives rise to in XPS. In [Fig. 2.3](#) a survey scan of $[\text{C}_8\text{C}_1\text{Im}][\text{Tf}_2\text{N}]$ is shown, along with the detailed core level spectra of all IL-related signals. The F 1s, O 1s and S 2p regions only show anion-related signals with BE values of ~ 689 , 532 and 169 eV, respectively. The asymmetric structure of the S 2p peak is due to the 2:1 spin-orbit splitting inherent to 2p orbitals, in the case of sulphur amounting to a peak separation of 1.2 eV. The C 1s and N 1s regions, however, contain multiple signals that can be assigned to both cation and anion and are therefore of utmost value when analysing the surface structure with regard to enrichment effects. More specifically, in the N 1s region two signals with a ratio of 2:1 are observed. The 402 eV feature is attributed to the two imidazolium nitrogens (exhibiting identical BE values irrespective of their slightly different chemical environment) and is therefore labelled N_{cation} . The peak around 399 eV originates from the imidic nitrogen of the anion and is accordingly named N_{anion} . For the C 1s region a more complicated structure is observed which shall be discussed in more detail in the following paragraph.

For $[\text{C}_8\text{C}_1\text{Im}][\text{Tf}_2\text{N}]$ three main features can be clearly distinguished in the C 1s region with BE values of ~ 293 , 287 and 285 eV. Due to the chemical structure of

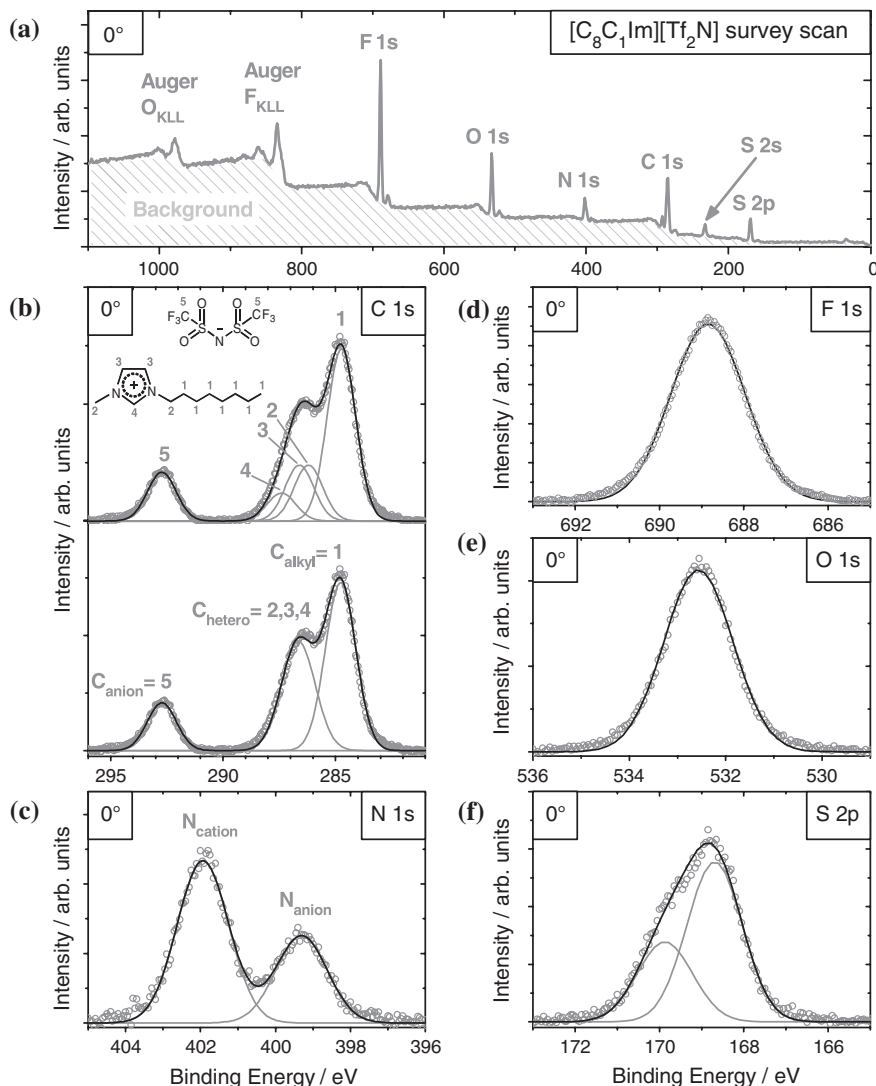


Fig. 2.3 Overview over XP survey (a) and core level spectra of $[\text{C}_8\text{C}_1\text{Im}][\text{Tf}_2\text{N}]$. In the C 1s region (b) two different fitting procedures are shown. The upper spectrum is fitted according to Ref. [23], while the latter portrays the fitting protocol used in this thesis (for details, please see text). In the C 1s spectrum three main features can be seen which correspond to aliphatic carbon (~ 285 eV; C_{alkyl}), carbon atoms bonded to nitrogen atoms (~ 287 eV; C_{hetero}) and the CF_3 groups of the anion (~ 293 eV; C_{anion}). In the N 1s region (c), two peaks are observed, of which the high BE signal corresponds to the two cationic nitrogen atoms (~ 402 eV; N_{cation}), while the low BE signal is attributed to the imidic nitrogen of the anion (~ 399 eV; N_{anion}). The F (~ 689 eV), O (~ 532 eV) and S (~ 169 eV) atoms (d–f) of the anion are all chemically equivalent and give rise to one single signal, whereas the S 2p signal is spin orbit split by 1.2 eV

the $[\text{C}_8\text{C}_1\text{Im}]^+$ cation four chemically non-equivalent carbon species are present (species 1–4, see Fig. 2.3). An additional carbon species is derived from the anion, resulting in five chemically different species (shown in the fit analysis of the upper C 1s spectrum of Fig. 2.3b). Due to the limited energy resolution all carbon species of the imidazolium ring bonded to nitrogen atoms give rise to the feature observed at ~ 287 eV. As is illustrated in the lower spectrum of Fig. 2.3b, we therefore coalesce these three species (2–4) into one carbon signal (slightly broader, see experimental section for details), labelled C_{hetero} . The high-BE feature is assigned to the CF_3 groups of the anion (5) and is accordingly called C_{anion} . The signal at ~ 285 eV originating from the aliphatic carbons (1) of the alkyl chain is named C_{alkyl} .

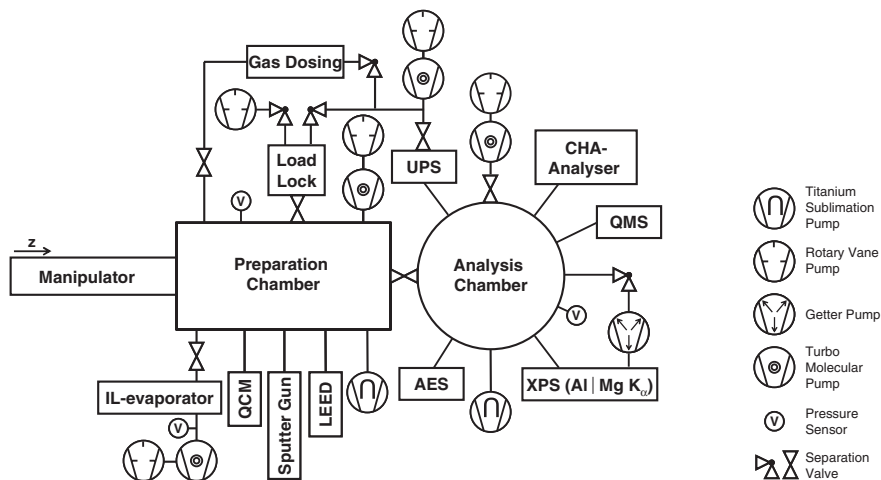
With this procedure an unambiguous assignment of all IL-related signals is achieved and will be used as presented here throughout this thesis. The subsumption of all C_{hetero} into one peak does not only allow for a very intuitive interpretation of ARXPS results but also yields a highly reliable quantitative analysis, which is partly due to the fact that the amount of fit constraints are reduced to a minimum.

2.3 The UHV Apparatus

The aim of this chapter is to introduce the reader to the UHV apparatus used in this thesis. The general setup of the chamber is explained and new additions and alteration made to the chamber are briefly discussed.

ESCALAB 200: The ESCALAB 200 system is a standard UHV chamber composed of an analysis chamber, a preparation chamber and a sample transfer system through which samples can be introduced into the UHV system. To the preparation chamber are fitted a sputter gun for sample cleaning by Ar^+ ion bombardment, an IL evaporator system and a quartz-crystal microbalance (QCM) for IL flux control. Furthermore, low energy electron diffraction (LEED) optics and a gas dosing system are attached. The analysis chamber is equipped with a concentric hemispherical electron energy analyser (CHA) for measuring the kinetic energy of the photoelectrons and a non-monochromatised dual anode X-ray gun generating either Al-K_α ($h\nu = 1486.6$ eV) or Mg-K_α ($h\nu = 1253.4$ eV) radiation. Furthermore, a UV lamp and an electron gun are attached for UP and Auger spectroscopy, while a quadrupole mass spectrometer allows for detection of desorbing species during heating or photon-induced desorption from the sample surface. The setup of the chamber is depicted in Scheme 2.3.

The general setup of the chamber in its original (analysis and load lock chamber) and modified (preparation chamber upgrade) state has been thoroughly discussed elsewhere [24, 25]. In the course of this thesis a few major modifications were made. Firstly, the old ESCALAB 200 MK II CHA was replaced by a new VG SCIENTA R3000 analyser. In addition, the former X-ray gun was replaced by a SPECS XR50 featuring an additional water-cooled shroud to minimize heat transfer from the x-ray anode to the sample surface. For IL thin film preparation a detachable IL evaporator system was installed, allowing for IL exchange and separate



Scheme 2.3 Diagram of the ESCALAB 200 spectrometer in its current state

baking of the evaporator unit. Finally, a new sample holder system was designed and installed meeting the specific needs for both the current and future IL research planned in our group. While the new CHA was characterized elsewhere [26], both the evaporator unit and the sample holder system will be reviewed below.

IL Evaporator: Compared to standard thermal evaporator systems, an IL evaporator has to meet a number of specific criteria to provide the desired performance. The most important aspects are that (i) the evaporator can be installed in a way, that the IL will not drip out, (ii) creeping of the IL inside the evaporator is avoided, (iii) the evaporator unit can be cooled during bake-out, as the IL evaporation temperature is in the range of the bake-out temperatures ($\sim 160^\circ\text{C}$), (iv) the evaporator unit can be attached and removed without venting the chamber. The above-mentioned criteria were satisfactorily met by choosing a setup as is displayed in Fig. 2.4.

For the evaporator unit a commercially available TECTRA WKC3 high temperature Knudsen cell was chosen, which has a cooling shroud and a tight-fitting shutter assembly. The shutter assembly was slightly modified by inserting an additional aperture to avoid excessive creeping of the IL within the evaporator. Detailed drawings and measurements of the evaporator unit as well as the modified parts can be found in the Appendix, Sect. A.1.1. Using a separate pumping unit and pressure sensor, a gate valve and a z-transfer on which the evaporator is mounted, the whole setup can be separated from the main chamber. This setup allows for separate baking of the evaporator (at moderate baking temperature $\leq 120^\circ\text{C}$) and fast IL refill/exchange. Temperature control is achieved by a type-K thermocouple linked to a EURO THERM 2261 PID controller. The evaporation rates are monitored using a QCM mounted on a rotatable feedthrough which can be pivoted directly into the IL beam.

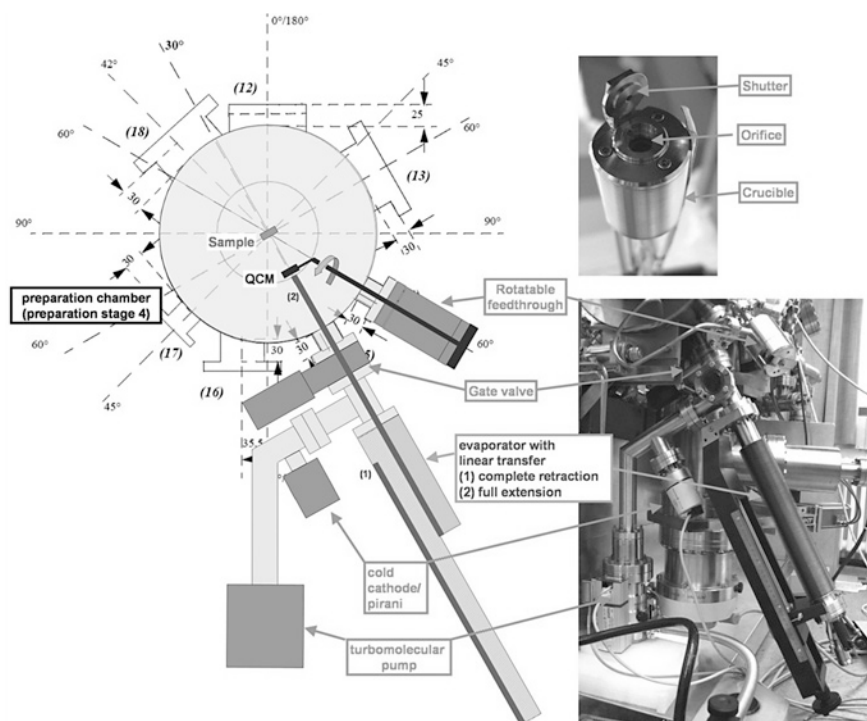


Fig. 2.4 Sketch and photo of the IL evaporator setup. With this setup the evaporator can be detached from the chamber, for refilling or change of IL. Furthermore, the IL can be introduced to the chamber after bake-out, which is a crucial point as the IL evaporation temperature lies in the range of the bake-out temperature

Sample Holder System: Certain improvements to the old sample holder system were necessary to successfully pursue future research goals. Regarding the old sample holder system, three main disadvantages occurred when using it for the IL research conducted in this work. Firstly, the absence of reliable temperature reading (thermo couple only mounted on the side of the manipulator head) directly on the sample was found to be a major drawback, as it is necessary to both accurately determine the IL temperature when heating or cooling the sample but also when annealing the single crystals used for the thin film experiments. A further disadvantage of the former system was that the sample was positioned rather loosely in the sample holder. Therefore, when tilting the sample to 80° , tipping of the sample sometime occurred leading to erroneous sample positions and reduced signal intensities. To summarize, the main requirements for a new sample holder system were found to be (i) reliable and fast sample transfer paired with a firm and reproducible sample position in the manipulator, (ii) stable and accurate temperature reading directly on the sample, (iii) the option to install a three electrode setup to be able to perform in situ electrochemistry in future projects, and (iv) the possibility to efficiently cool (good

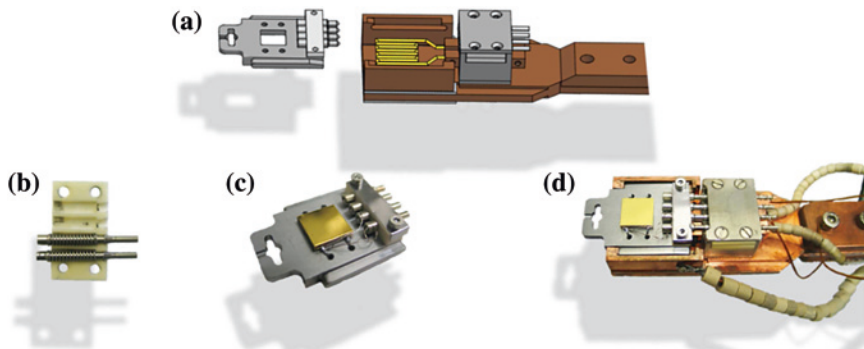


Fig. 2.5 Sketch (a) and pictures (b–d) of the sample holder system. The pins on the sample holder and the spring-loaded counter-notches (b) fitted to the manipulator head are made of type K thermocouple material. Once inserted into the manipulator, the springs push the sample holder back into its locked position (c), which guarantees both good electrical contact as well as firm and accurate mechanical interlock

thermal contact to LN_2 cooling of manipulator) and heat (both heating filament and electron bombardment for high-temperature annealing) the sample. After assessing the requirements a completely new design of sample holder, manipulator head and transfer system was developed. In the sample holder setup presented in Fig. 2.5 all of these requirements are met satisfactorily. By using the pin-shaped spring contact two major issues—firm mechanical interlock and both thermocouple and electric connection of the sample—could be solved at once. The sample transfer system offers an easy yet reliable and robust transfer mechanism. Compared to the former sample holder system cooling is much more efficient, resulting in sample temperatures as low as 90 K (using liquid nitrogen as cooling agent) as compared to 130 K achieved with the old sample holder. Also, electron beam heating works much more reliably with the new sample holder system, where in first tests with a Ni(111) single crystal temperatures of ~ 1200 K could be achieved easily. The detailed construction drawings are compiled in the Appendix section, Sect. A.1.2.

2.4 Experimental Aspects

Throughout this thesis a variety of different sample preparation methods as well as different analysis methods and UHV components were used. Therefore, specific experimental aspects are provided in the corresponding sections. In addition, a few fundamental experimental aspects will be discussed to give the reader a basic insight into the methods employed.

Ionic Liquids: In this work a variety of ILs were used, therefore an overview of all ILs studied is given in Table 2.1. $[\text{C}_8\text{C}_1\text{Im}][\text{Tf}_2\text{N}]$, $[\text{C}_8\text{C}_1\text{Im}][\text{Pf}_2\text{N}]$, $[\text{C}_8\text{C}_1\text{Im}]\text{Cl}$, $[\text{C}_2\text{C}_1\text{Im}][\text{Tf}_2\text{N}]$, and $[\text{C}_1\text{C}_1\text{Im}][\text{Tf}_2\text{N}]$ were synthesized under

ultra-clean conditions by Natalia Paape in the laboratories of Peter Wasserscheid. $[\text{C}_8\text{C}_1\text{Im}]$ was provided by Alasdair Taylor from the Licence group at University of Nottingham, while $[\text{C}_8\text{C}_1\text{Im}][\text{NO}_3]$ was synthesized by Ralf Lungwitz from the Spange group at University of Chemnitz. The above-mentioned ILs were synthesized under the premise of utmost purity and characterized by a variety of spectroscopic methods, including NMR spectroscopy, Karl-Fischer titration, thermal gravimetric analysis (TGA), and density and viscosity measurements. The ILs $[\text{C}_8\text{C}_1\text{Im}][\text{FAP}]$, $[\text{C}_8\text{C}_1\text{C}_1\text{Im}][\text{Tf}_2\text{N}]$ and $[\text{C}_8\text{C}_1\text{C}_1\text{Im}]\text{Br}$ were kindly given by Merck, while $[\text{C}_8\text{C}_1\text{Im}]\text{Br}$ and $[\text{C}_8\text{C}_1\text{Im}][\text{PF}_6]$ were purchased therefrom. $[\text{C}_8\text{C}_1\text{Im}][\text{BF}_4]$ and $[\text{C}_8\text{C}_1\text{Im}][\text{TfO}]$ were purchased from Sigma-Aldrich, whereas $[\text{C}_4\text{C}_1\text{Pyr}][\text{Tf}_2\text{N}]$ was purchased from IoLiTec. The Merck-ILs were synthesized in small batches, also enforcing ultra-clean standards [27]. The ILs from Sigma Aldrich had specified purities of >95 % for $[\text{C}_8\text{C}_1\text{Im}][\text{BF}_4]$ and >97 % for $[\text{C}_8\text{C}_1\text{Im}][\text{TfO}]$, while the IoLiTec IL was specified as >99 % pure. All ILs were used as obtained.

Sample Preparation: In the following a brief introduction to the standard sample preparation procedures is given. Detailed aspects or specific preparation steps for particular experiments are provided within the corresponding chapters.

Ionic liquid films: Macroscopically thick IL films (thickness ~ 0.1 mm) were prepared by depositing the corresponding IL onto a planar gold foil, which had previously been treated with acetone and isopropanol in an ultrasonic bath, and had been stored in an oven at 70 °C for drying [28]. In the load lock chamber of the XPS apparatus the IL samples were carefully degassed at a pressure of $\sim 1 \times 10^{-6}$ mbar to remove residual water and other possible volatile impurities [5].

Single crystal surfaces: The Au(111) and Ni(111) single crystals were both purchased from MATECK GmbH, with specified purities of 99.999 and 99.99 %, respectively. Both crystals were polished on one side and aligned to the (111) plane to better than 0.1°. They were both of square shape with dimensions of $11 \times 11 \times 2$ mm³, with spark-eroded holes along two sides allowing for sample mounting with Ta wires as is shown in Fig. 2.5 and Ref. [26]. For the Au(111) single crystal sample preparation was performed by sputtering the sample with 600 V Ar⁺ ions followed by annealing to 800–900 K for 5 min. The Ni(111) was sputtered with 1 kV Ar⁺ ions and heated to 1100–1200 K for about 1 min. To avoid surface segregation of sulphur during the cooling process, the Ni(111) sample was additionally cooled with LN₂. Surface cleanliness was checked with XPS, while long range order of the surface was monitored with LEED, where for Au(111) the typical $(23 \times \sqrt{3})$ “herringbone” superstructure was observed. For clean Ni(111) very sharp (1×1) reflexes without superstructure were observed.

Suprasil glass samples: Suprasil 300 fused silica samples were kindly provided by M. Scharrer from the MPI Erlangen. They were obtained from HERAEUS as 1 mm thick disks of $d = 25$ mm and fitted to the sample holder by cutting down to dimensions of 15×12 mm². This was followed by thorough cleaning with acetone and isopropanol in an ultrasonic bath and storing in an oven at 70 °C until further use. All subsequent surface modifications carried out are specifically

discussed in Chap. 5. For mounting the samples on a sample holder, tantalum strips were used as is shown in Ref. [26].

Thin film preparation: IL thin film deposition was achieved by thermal evaporation of the respective IL using the evaporator setup discussed above. After degassing the empty evaporator crucible at 1200 K, the IL was introduced into a pyrolytic boron nitride (PBN) crucible and fitted to the evaporator. The evaporator unit was slowly pumped down with open shutter followed by moderate baking ($T \leq 120$ °C) while simultaneously “cooling” the crucible with 60 °C hot water. After bake-out the evaporator was held at 380 K for at least 4 h to degas the IL, again with the shutter opened. During IL deposition the temperature was set between 420 and 440 K, depending on IL and desired evaporation rate (see Sect. 4.2 for details). Deposition rates were estimated using the attenuation (damping) of the Au 4f XPS signal of the Au(111) single crystal. Consistency of the deposition rate was regularly monitored with QCM measurements.

XPS measurements and data evaluation: General aspects relevant for all studies of this thesis are discussed in the following, while procedures only relevant to individual chapters are discussed therein.

XPS measurements: XP spectra were taken with a VG ESCALAB 200 spectrometer using non-monochromatised Al- K_{α} radiation ($h\nu = 1486.6$ eV). For the core-level spectra pass energies were set to low enough values (depending on which analyser was used, as will be specified in the respective chapters), so that the resulting overall resolution of ~ 0.9 eV was given mainly by the natural line width of the non-monochromatised Al- K_{α} radiation. At the kinetic energies used (800–1400 eV) the inelastic mean free path (IMFP) of photoelectrons in organic compounds is in the range 2–3 nm [8]. Therefore, measurements at 0° average over several ion layers of the near-surface region (information depth, ID: 5–9 nm, depending on the kinetic energy), while for 80° emission the surface sensitivity is enhanced by a factor of six resulting in an information depth of around 1–1.5 nm, with the majority of the signal originating from within the first molecular layer.

Data evaluation: For the two different CHA analysers slightly different data analysis procedures were used. For the old analyser, the spectra were directly imported into Origin 7.5 and fitted using Gaussian functions after linear background subtraction. For the new R3000 analyser, the raw data were analysed with the Casa XPS software, where for peak fitting a combination of Gaussian and Lorentzian lineshape at a ratio of 70:30 was used, leading to slightly better fits without affecting the quantitative analysis; indeed, within the margins of error, both methods provided identical results for quantitative analysis done in this thesis. For $[C_8C_1Im]^+$ ILs the C 1s spectra were fitted with the constraint of full width half-maximum, $fwhm(C_{hetero}) = 1.11 \times fwhm(C_{alkyl})$, in accordance with previously published results [10]. In some case, as will be specified were it applies, it was necessary to account for slight charging phenomena (± 0.15 eV), which have been observed and discussed previously [29]. Therefore, the spectra were shifted in a way that $BE(C_{alkyl}) = 285.0$ eV. Please see Sect. 3.1 for a detailed discussion. For film thickness calculations a constant value of 3 nm for

the IMFP of the recorded photoelectrons was assumed for systems where the kinetic energy of the photoelectron is ~ 1200 eV (Au 4f and Si 2p), according to Ref. [8]. For kinetic energies well below 1000 eV (such as the Ni2p signal, $E_{\text{kin}} \sim 640$ eV), however, the IMFP value of 3 nm was adjusted by dividing by a factor of 1.83 (as estimated from IMFP calculations for organic materials for 1200 and 650 eV, see Ref. [7]), which provided reliable results.

References

1. A. Einstein, Ann. Phys. **322**, 132 (1905)
2. S. Hüfner, *Photoelectron Spectroscopy* (Springer-Verlag, Berlin Heidelberg New York, 1995)
3. M. Henzler, W. Göpel, *Oberflächenphysik des Festkörpers* (Teubner, Stuttgart, 1994)
4. G. Ertl, J. Küppers, *Low Energy Electrons and Surface Chemistry* (VCH, Weinheim, 1985)
5. C. Kolbeck, M. Killian, F. Maier, N. Paape, P. Wasserscheid, H.-P. Steinrück, Langmuir **24**, 9500 (2008)
6. D. Briggs, M.P. Seah, *Practical Surface Analysis* (Springer-Verlag, Berlin, 1990)
7. S. Tanuma, C.J. Powell, D.R. Penn, Surf. Interf. Anal. **21**, 165 (1994)
8. R.F. Roberts, D.L. Allara, C.A. Pryde, D.N.E. Buchanan, N.D. Hobbins, Surf. Interf. Anal. **2**, 5 (1980)
9. D.C. Jackson, T.E. Gallon, A. Chambers, Surf. Sci. **36**, 381 (1973)
10. K.R.J. Lovelock, C. Kolbeck, T. Cremer, N. Paape, P.S. Schulz, P. Wasserscheid, F. Maier, H.-P. Steinrück, J. Phys. Chem. B **113**, 2854 (2009)
11. S. Boghosian, R. Fehrmann, N.J. Bjerrum, G.N. Papatheodorou, J. Catal. **119**, 121 (1989)
12. P. Walden, Bull. Acad. Impér. Sci. St. Pétersbourg **8**, 405 (1914)
13. J.S. Wilkes, J.A. Levisky, R.A. Wilson, C.L. Hussey, Inorg. Chem. **21**, 1263 (1982)
14. J. Wilkes, Chem. Commun. **13**, 965 (1992)
15. A.E. Visser, R.P. Swatloski, W.M. Reichert, R. Mayton, S. Sheff, A. Wierzbicki, J.H. Davis, R.D. Rogers, Chem. Commun. **37**, 135 (2001)
16. P. Wasserscheid, W. Keim, Angew. Chem. Int. Ed. **39**, 3772 (2000)
17. S. Zahn, F. Uhlig, J. Thar, C. Spickermann, B. Kirchner, Angew. Chem. Int. Ed. **47**, 3639 (2008)
18. N.V. Plechkova, K.R. Seddon, Chem. Soc. Rev. **37**, 123 (2008)
19. J.N.C. Lopes, A.A.H. Padua, J. Phys. Chem. B. **110**, 3330 (2006)
20. T.L. Amyes, S.T. Diver, J.P. Richard, F.M. Rivas, K. Toth, J. Am. Chem. Soc. **126**, 4366 (2004)
21. P. Nockemann, B. Thijs, S. Pittois, J. Thoen, C. Glorieux, K. Van Hecke, L. Van Meervelt, B. Kirchner, K. Binnemans, J. Phys. Chem. B **110**, 20978 (2006)
22. P. Wasserscheid, T. Welton, *Ionic liquids in synthesis*, 2nd edn. (Wiley-VCH, Weinheim, 2008)
23. O. Höfft, S. Bahr, M. Himmerlich, S. Krischok, J.A. Schäfer, V. Kempter, Langmuir **22**, 7120 (2006)
24. M. Probst, PhD Thesis, Friedrich-Alexander-University Erlangen-Nuremberg, 2003
25. F. Grellner, PhD Thesis, Friedrich-Alexander-University Erlangen-Nuremberg, 1993
26. M. Stark, Master Thesis, Friedrich-Alexander-University Erlangen-Nuremberg, 2010
27. Personal Communication, M. Watermann, Merck KGaA, Darmstadt, 2009
28. T. Cremer, Diploma Thesis, Friedrich-Alexander University Erlangen-Nuremberg, 2008
29. E.F. Smith, F.J.M. Rutten, I.J. Villar-Garcia, D. Briggs, P. Licence, Langmuir **22**, 9386 (2006)

Ionic Liquid Bulk and Interface Properties
Electronic Interaction, Molecular Orientation and
Growth Characteristics

Cremer, T.

2013, XII, 170 p., Hardcover

ISBN: 978-3-319-00379-5